Model and trajectory optimization for an ideal laser-enhanced solar sail

Carzana, Livio; Dachwald, Bernd; Noomen, Ron

Publication date
2017

Document Version
Final published version

Published in
68th International Astronautical Congress, IAC 2017

Citation (APA)
Carzana, L., Dachwald, B., & Noomen, R. (2017). Model and trajectory optimization for an ideal laser-enhanced solar sail. In *68th International Astronautical Congress, IAC 2017: Unlocking Imagination, Fostering Innovation and Strengthening Security* (Vol. 2, pp. 874-885). International Astronautical Federation, IAF.

(Preprint) AAS 22-715

A NEW MODEL FOR THE PLANETARY RADIATION PRESSURE ACCELERATION FOR SOLAR SAILS

Livio Carzana,[*] Pieter Visser,[†] and Jeannette Heiligers[‡]

Solar sailing is a propellantless propulsion method that takes advantage of solar radiation pressure to generate thrust. The last decades have seen the launch of several solar-sail missions to demonstrate the technology's potential for space exploration and exploitation. Even more missions are scheduled for launch in the near future, including NASA's ACS3 and NEA Scout missions and Gama's Alpha sailcraft. Although most of these sailcraft have flown – or will fly – in LEO, where the planetary radiation pressure is strong (up to approximately 20% of the solar radiation pressure), studies on the perturbing accelerations produced by the Earth's albedo and blackbody radiation have been conducted only to a very limited first-order extent. This paper therefore provides a novel, detailed analytical model for these perturbing accelerations, valid for double-sided perfectly reflecting solar sails. The underlying assumptions of the model are presented and its full derivation is described. A thorough analysis of the blackbody and albedo radiation pressure accelerations is conducted for a variety of orbital conditions and Sun-Earth-sail configurations. In order to quantify the accuracy of the model, a comparison with the state of the art (the finite-disk radiation source model) is provided. Ultimately, a variety of analyses to quantify the effect of Earth's albedo and blackbody radiation on the maneuvering capabilities of solar sails are provided, using the orbit of the ACS3 mission as reference scenario. These analyses show that, for an orbit-raising steering law, losses in the altitude gain of 19.6% of the total gain are incurred over a 10-day orbit-raising period. Similarly, losses in the inclination gain of up to 25% of the total gain are observed when implementing an inclination-changing steering law. These results highlight the non-negligible effect of uncontrolled planetary radiation pressure acceleration on the maneuvering capabilities of solar sails in LEO.

INTRODUCTION

Solar sailing is a low-thrust propulsion method that has raised increasing amounts of interest over the last few decades, mainly because of its propellantless nature[1]. In light of its enabling potential for a wide variety of mission scenarios[2,3], extensive research has been conducted on its dynamics and trajectory optimization, while several solar-sail missions have flown to increase its technology readiness level and mission applicability. Although most of the studies on the topic have been conducted for heliocentric flight regimes, the majority of solar-sail missions to date

---

[*] PhD candidate, Faculty of Aerospace Engineering, Delft University of Technology, Kluyverweg 1, 2629 HS Delft.

[†] Full Professor, Faculty of Aerospace Engineering, Delft University of Technology, Kluyverweg 1, 2629 HS Delft.

[‡] Assistant Professor, Faculty of Aerospace Engineering, Delft University of Technology, Kluyverweg 1, 2629 HS Delft.

remained Earth-bound, as will those scheduled for launch in the near-future, e.g., NASA's Advanced Composite Solar Sail System (ACS3)[4] and NEA Scout[5] missions and Gama's Alpha mission. In close proximity of the Earth, the dynamics are much more complex than in interplanetary space because of the presence of eclipses, atmospheric drag, and planetary radiation pressure (PRP). While multiple studies on the effect of aerodynamic drag in Low Earth Orbit (LEO) have been conducted and showed the enabling capabilities of solar sails for deorbiting purposes[6,7,8,9], optimal orbit raising[10,11], and optimal inclination changing[10,12], the accurate derivation of the PRP acceleration and the perturbing effect on the solar-sail dynamics have been investigated to a much lesser extent. The research conducted on this topic to date has mainly focused on the first-order characterization of the blackbody radiation pressure (BBRP) and albedo radiation pressure (ARP) accelerations and the optimization of planetocentric solar-sail trajectories under these effects[13,14]. In these studies, the models considered for the BBRP and ARP accelerations are based on the one first devised by McInnes[1] and assume the radiating body to be a uniformly bright disk irradiating only in the planet-to-sailcraft direction. While these assumptions correctly approximate the PRP acceleration experienced by solar sails at large distances from Earth, at low altitudes a more realistic geometry of the problem should be considered to achieve accurate results. It should be noted that other studies considering a more complex geometry of the Earth have also been conducted[15,16,17], in which the Earth is modeled as an isotropic, spherical radiation source. However, these only investigated the radiative power received by a flat plate in Earth orbit, without deriving the corresponding radiation pressure and acceleration exerted. The need for determining an accurate expression for the PRP acceleration in proximity of the Earth arises from the fact that the PRP acceleration can reach a non-trivial magnitude in the order of 10-20% of the solar-sail characteristic acceleration[13] (depending on the orbital altitude and solar-sail attitude). Consequently, a realistic PRP acceleration model is warranted and would also lay the basis for the accurate optimization of Earth-bound steering strategies taking advantage of both the SRP and PRP accelerations.

In light of the above, this paper presents a novel and detailed analytical model for the BBRP and ARP accelerations. Unlike any other analytical PRP acceleration model available in the literature, the model presented in this paper accounts for the complex geometry of the problem in its entirety. Indeed, it considers the spherical shape of the emitting body (i.e., the Earth), accounts for the limited area of the radiating surface as seen from the sailcraft, the illumination conditions of the radiating surface, and the possibility that both sides of the sail are exposed to the planetary radiation. This model – hereinafter referred to as "spherical" model – is an extension of the finite-disk (FD) radiation pressure acceleration model devised by McInnes[1], is valid at any altitude, and can be used for flat-shaped, two-sided reflective solar sails, i.e., solar sails with perfectly reflecting front and back sides. The assumptions and full derivation of the model are presented and thoroughly described. Analyses are performed to quantify the magnitude of the BBRP and ARP accelerations for different altitudes, sail attitudes, and Sun-planet-sailcraft angles. In order to quantify the accuracy of the model, a comparison with the FD model is provided. Ultimately, a variety of analyses are conducted to assess the effect of the PRP accelerations on the maneuvering capabilities of solar sails in Earth orbit. To that end, the solar-sail orbital dynamics are propagated under the influence of SRP, atmospheric drag, and PRP. During the propagation, locally optimal orbit-raising and inclination-changing steering laws are employed, which are computed using an algorithm accounting for both SRP and atmospheric drag in the optimization process[10]. By analyzing the results achieved with and without PRP acceleration in the dynamics, the impact of the uncontrolled PRP acceleration on the maximum achievable altitude and inclination changes is quantified. The analyses are performed considering NASA's ACS3 mission as reference scenario[4,10]. This solar-sail mission is scheduled for launch in early 2023 and is used in this paper to demonstrate the effect of the PRP perturbation on the solar-sail orbital dynamics, particularly in LEO.

DYNAMICAL MODEL

The equations of motion describing the dynamics of a solar sail in Earth-bound orbit are expressed in an inertial Earth-centered reference frame, $I(x, y, z)$, with the x-axis pointing towards the vernal equinox, the z-axis perpendicular to the equatorial plane and pointing towards the north pole, and the y-axis completing the right-handed frame. Within this frame the equations of motion of a flat, perfectly reflecting solar sail under the influence of SRP, atmospheric drag, BBRP, and ARP can be expressed in vectorial form as:

$$\ddot{\boldsymbol{r}} + \frac{\mu}{r^3}\boldsymbol{r} = \boldsymbol{a}_{SRP} + \boldsymbol{a}_{aero} + \boldsymbol{a}_{BBRP} + \boldsymbol{a}_{ARP} \tag{1}$$

where the dot notation indicates differentiation with respect to time, $\boldsymbol{r} = [x, y, z]^T$ is the sailcraft position vector, $r = ||\boldsymbol{r}||$, $\mu = 398600.4415$ km^{3}s^{-2} is the Earth gravitational parameter[18], and $\boldsymbol{a}_{SRP}$, $\boldsymbol{a}_{aero}$, $\boldsymbol{a}_{BBRP}$, and $\boldsymbol{a}_{ARP}$ are the SRP, aerodynamic, BBRP, and ARP accelerations, respectively. These accelerations will be described in more detail in the following sections.

It should be noted that the gravitational acceleration due to the Earth's J_2 spherical harmonics coefficient – as well as other gravitational perturbations of smaller magnitude – are not considered in this paper. This choice is justified by the fact that, in the analyses presented, only steering laws to increase the semi-major axis and inclination are considered. The J_2 perturbation has no secular effect on these Keplerian elements, only a short-term periodic effect[18]. Therefore, even though the J_2 acceleration can become as large as 460 times the ACS3's characteristic acceleration[*], including this acceleration in the dynamics would only add significant noise to the results. Gravitational perturbations of smaller magnitude with a secular effect on the inclination exist, such as the gravitational accelerations of the Moon and the Sun. However, these have also not been considered in the right-hand side of Eq. (1) for the same reason. They add noise that hampers a clear investigation into the effects of the BBRP and ARP accelerations on the solar-sail orbital dynamics.

Solar Radiation Pressure Acceleration

The SRP acceleration is defined as[1]:

$$\boldsymbol{a}_{SRP} = \nu a_c \cos^2(\alpha)\hat{\boldsymbol{n}} \tag{2}$$

where $\nu \in [0, 1]$ is the shadow factor and $\alpha \in [0, \pi/2]$ is the solar-sail cone angle measured between the direction of sunlight, $\hat{\boldsymbol{l}}$, and the sail normal direction with no component pointing towards the Sun, $\hat{\boldsymbol{n}}$, see Figure 1a. The shadow factor ν accounts for the effect of eclipses and its value ranges from 0 (no sunlight reaches the sail) to 1 (sail completely illuminated). In this paper, eclipses are modeled with a conical shadow model similar to the one presented in References 19 and 20, with the only difference that $\nu = 0$ both when in umbra and penumbra. a_c represents the SRP characteristic acceleration, i.e., the maximum SRP acceleration (achieved for $\alpha = 0$) at a distance of 1 AU from the Sun[1]:

$$a_c = \frac{2\mathbb{S}_{\oplus}}{c\sigma} \tag{3}$$

---

[*] The characteristic acceleration is the maximum SRP acceleration achievable by a perfectly-reflecting solar sail at 1 AU from the Sun.

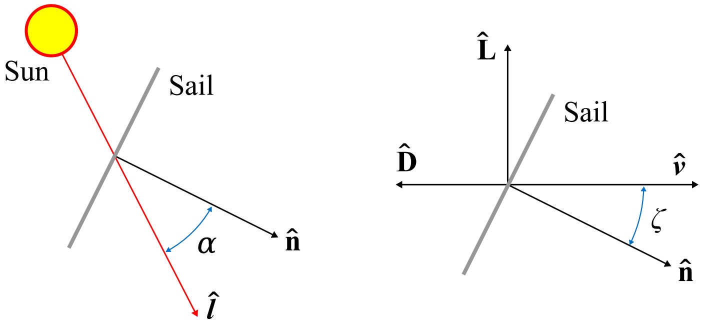

(a) (b)

Figure 1. Solar-sail cone angle, α, and complementary angle to the angle of attack, ζ.

In Eq. (3), $\mathbb{S}_\oplus$ = 1367 Wm^{-2} represents the solar flux at Earth[18], c = 299792.458 km s^{-1} is the speed of light in vacuum[21], and σ is the sailcraft mass-to-sail area ratio.

Aerodynamic Acceleration

The aerodynamic acceleration is modeled based on the aerodynamics of a flat plate[10,11,12] as:

$$\boldsymbol{a}_{aero} = \frac{\rho v^2}{2\sigma}(C_D\hat{\mathbf{D}} + C_L\hat{\mathbf{L}}) \tag{4}$$

where C_D and C_L are the drag and lift coefficients of the sail, $\hat{\mathbf{D}}$ and $\hat{\mathbf{L}}$ are the drag and lift directions (see Figure 1b), v is the sailcraft inertial velocity, and ρ is the atmospheric density, which is modeled using an averaging technique based on the NRLMSISE-00 atmospheric model[10]. The expressions for C_D and C_L are given by[10,11,12]:

$$C_D = 2\left[\sigma_T + \sigma_N V_R\left|\cos\zeta\right| + \left(2-\sigma_N-\sigma_T\right)\cos^2\zeta\right]\left|\cos\zeta\right| \tag{5}$$

$$C_L = 2\left[\sigma_N V_R + \left(2-\sigma_N-\sigma_T\right)\left|\cos\zeta\right|\right]\left|\cos\zeta\right|\sin\zeta \tag{6}$$

where $\zeta \in [0, \pi/2]$ is the complementary angle to the solar sail's angle of attack (again, see Figure 1b), σ_N and σ_T represent the normal and tangential momentum accommodation coefficients, respectively, and V_R is the ratio of the atmospheric particle average thermal velocity to the sailcraft inertial velocity. Based on References 10 and 22, $\sigma_N = \sigma_T = 0.8$, $V_R = 0.05$.

Planetary Radiation Pressure Acceleration

In order to determine the PRP acceleration exerted on a solar sail, it is essential to first establish the amount of planetary radiation received by the sail, define its flux and finally the radiation pressure. If an elementary piece of Earth's surface dA is considered, see Figure 2a, the amount of power irradiated in a generic direction $\hat{\boldsymbol{s}}$ and enclosed within an infinitesimal solid angle $d\Omega$ is represented by the second differential d^2P as[23]:

$$d^2P = I\cos(\vartheta)d\Omega dA \tag{7}$$

In Eq. (7), I represents the planetary radiation intensity (across the entire electromagnetic spectrum) along the normal direction to dA, $\hat{\boldsymbol{N}}$, and $\vartheta \in [0, \pi/2]$ is the angle between $\hat{\boldsymbol{N}}$ and $\hat{\boldsymbol{s}}$, see again Figure 2a. When only the radiation received by the solar sail is considered, $d\Omega$ represents the solid angle subtended by an infinitesimal piece of illuminated sail surface, dS. In this case, $d\Omega$ is defined as[15]:

$$d\Omega = \frac{dS\cos(\theta)}{s^2} \tag{8}$$

where $\theta \in [0, \pi/2]$ is the angle between $\hat{\boldsymbol{s}}$ and the sail normal direction pointing away from the Earth, $\hat{\boldsymbol{n}}_{out}$, and s is the magnitude of the vector $\boldsymbol{s}$ pointing from dA to dS, see Figure 2a and 2b. Since this paper considers a flat-shaped solar sail whose dimensions are significantly smaller than s, θ and s can be assumed to be constant across the entire sail surface. This assumption allows to substitute Eq. (8) into Eq. (7) and integrate the latter with respect to dS over the entire sail surface, S. Performing the integration yields the radiation power dP received by the entire sail due to the radiation emitted by dA:

$$dP = I \cos(\vartheta) \frac{S \cos(\theta)}{s^2} dA \tag{9}$$

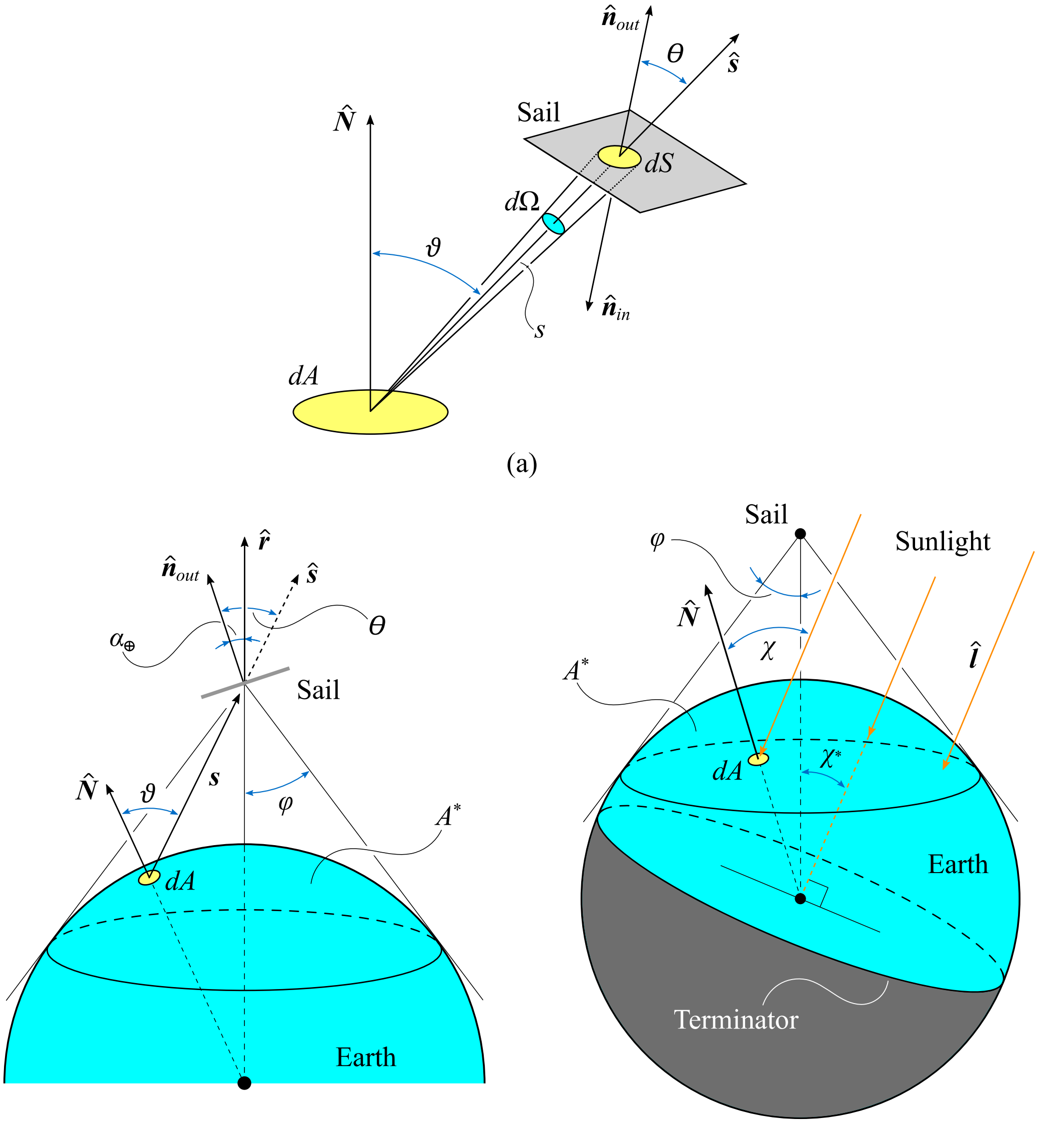

(a)

(b)

(c)

Figure 2. Geometry of the problem to determine the BBRP and ARP accelerations exerted on a solar sail.

The power flux at the sail's location due to the radiation emitted by dA, $d\mathbb{S}$, is then found as:

$$d\mathbb{S} = \frac{dP}{S\cos(\theta)} = I\frac{\cos(\vartheta)}{s^2}dA \tag{10}$$

The corresponding radiation pressure $d\mathbb{P}$ is given by[1]:

$$d\mathbb{P} = \frac{d\mathbb{S}}{c} = \frac{I}{c}\frac{\cos(\vartheta)}{s^2}dA \tag{11}$$

and the acceleration of the sail is[1]:

$$d\boldsymbol{a}_{PRP} = 2\frac{d\mathbb{P}}{\sigma}\cos^2(\theta)\hat{\boldsymbol{n}}_{out} = \frac{2I}{c\sigma}\frac{\cos(\vartheta)\cos^2(\theta)}{s^2}dA\,\hat{\boldsymbol{n}}_{out} \tag{12}$$

Ultimately, in order to find the total acceleration exerted on the sailcraft, Eq. (12) needs to be integrated over the entire visible surface of the Earth as seen from the sailcraft, A^*, yielding:

$$\boldsymbol{a}_{PRP} = \frac{2}{c\sigma}\hat{\boldsymbol{n}}_{out}\int_{A^*} I\frac{\cos(\vartheta)\cos^2(\theta)}{s^2}dA \tag{13}$$

The solution to the surface integral of Eq. (13) depends on the Earth-sail geometrical configuration and, most importantly, on the definition of the planetary radiation intensity, *I*. Indeed, the planetary radiation intensity quantifies the amount of radiation emitted by the surface elements dA across A^* and its definition depends on whether the blackbody or albedo radiation is considered. For the sake of clarity, hereinafter the symbols I_{BBRP} and I_{ARP} will be used when referring specifically to the blackbody and albedo radiation intensities, respectively. When the radiation intensity *I* does not vary across the visible surface A^*, an analytical solution to the surface integral of Eq. (13) can be found. In this case, the following expression for the PRP acceleration is obtained:

$$\boldsymbol{a}_{PRP} = a_{c,PRP}G_F\hat{\boldsymbol{n}}_{out} \tag{14}$$

where $a_{c,PRP}$ is the PRP characteristic acceleration and $G_F \in [0,1]$ is a so-called geometrical factor. The PRP characteristic acceleration is given by:

$$a_{c,PRP} = \frac{4\pi}{3}\frac{I}{c\sigma} \tag{15}$$

and similar to the "traditional" SRP characteristic acceleration, a_c, it represents the maximum achievable PRP acceleration. Note that hereinafter the symbols $\boldsymbol{a}_{BBRP}$ and $\boldsymbol{a}_{ARP}$ will be used instead of $\boldsymbol{a}_{PRP}$ – and, similarly, $a_{c,BBRP}$ and $a_{c,ARP}$ will be used instead $a_{c,PRP}$ – when the BBRP and ARP accelerations are considered, respectively. The geometrical factor correlates the Earth-sail geometrical configuration to the PRP acceleration and is defined as:

$$G_F = \frac{3}{2\pi}\int_{A^*}\frac{\cos(\vartheta)\cos^2(\theta)}{s^2}dA \tag{16}$$

The solution to the surface integral on the right-hand side of Eq. (16) depends on the geometrical configuration of the sail with respect to the Earth, which is uniquely identified by the planetary cone angle (PCA), $\alpha_{\oplus} \in [0, \pi/2]$, and maximum view angle, $\varphi \in [0, \pi/2]$, see Figure 2b. The former is defined as the angle between $\hat{\boldsymbol{n}}_{out}$ and the radial direction, $\hat{\boldsymbol{r}}$, while the latter is the angle between the direction pointing to the Earth's tangent as seen from the sailcraft and $-\hat{\boldsymbol{r}}$. Two possible configurations can then be defined:

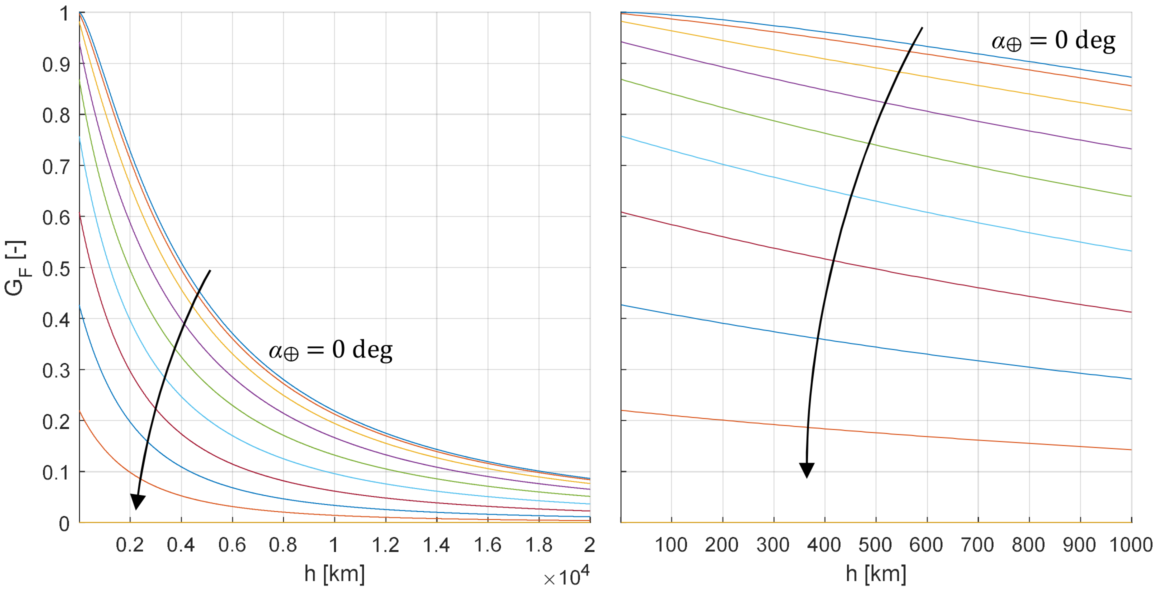

Figure 3. Geometrical factor as a function of altitude for different PCAs. The PCA increases in the direction of the arrow from 0 to 90 deg with a step size of 10 deg.

a) If $\alpha_\oplus + \varphi \leq \pi/2$, the incoming radiation from the visible surface A^* illuminates only one side of the sail. In this case, the geometrical factor is found as:

$$G_F\left(r,\alpha_\oplus\right) = 1-\sqrt{1-\frac{R^2}{r^2}}\left[1-\frac{R^2}{r^2}\left(1-\frac{3}{2}\sin^2(\alpha_\oplus)\right)\right] \tag{17}$$

where $R = 6378.1363$ km is the Earth radius[18].

b) If $\alpha_\oplus + \varphi > \pi/2$, the incoming radiation from the visible surface A^* illuminates both sides of the sail. In this case, each of the two sides of the double-sided reflecting sail provides an acceleration that points either along $\hat{\boldsymbol{n}}_{out}$ or in opposite direction, $\hat{\boldsymbol{n}}_{in} = -\hat{\boldsymbol{n}}_{out}$. Consequently, G_F assumes a more complex expression, given by:

$$\begin{aligned} G_F\left(r,\alpha_\oplus\right) = 1-\frac{1}{\pi}\Bigg\{ & 2\sqrt{1-\frac{R^2}{r^2}}\left[1-\frac{R^2}{r^2}\left(1-\frac{3}{2}\sin^2(\alpha_\oplus)\right)\right]\sin^{-1}\left(A\right)+2\tan^{-1}\left(B\right) \\ & -3B^3\cos^4(\alpha_\oplus)-2B\cos^2(\alpha_\oplus)\left(1-\frac{3}{2}\sin^2(\alpha_\oplus)\right)\Bigg\} \end{aligned} \tag{18}$$

where:

$$A = \frac{\cos(\alpha_\oplus)}{\sin(\alpha_\oplus)}\sqrt{\frac{r^2}{R^2}-1} \quad ; \quad B = \sqrt{\frac{R^2}{r^2\cos^2(\alpha_\oplus)}-1} \tag{19}$$

In Figure 3, the geometrical factor is plotted as a function of the orbital altitude, h, for a range of different PCAs. This plot can be used by the reader to easily retrieve the value of G_F for a wide range of Earth-sail geometrical configurations and directly compute the corresponding PRP acceleration through Eq. (14).

To determine the BBRP and ARP accelerations, the definitions of the blackbody and albedo radiation intensities, I_{BBRP} and I_{ARP}, are required. These are provided in the following subsections.

Blackbody Radiation Intensity. When the blackbody radiation is considered, the radiation intensity, I_{BBRP}, is constant and is given by[24]:

$$I_{BBRP} = \frac{\sigma_{SB} T^4}{\pi} \tag{20}$$

where $\sigma_{\mathrm{SB}} = 5.670374419 \cdot 10^{-8}$ Wm^{-2}K^{-4} is the Stefan-Boltzmann constant[21] and $T = 249.21$ K is the blackbody temperature of the Earth, computed by imposing the planetary energy balance. Because I_{BBRP} does not vary across the visible surface A^*, Eq. (14) can be used directly to compute the BBRP acceleration, $\boldsymbol{a}_{BBRP}$. In particular, the geometrical factor can be found through Eq. (17)-(19), whereas the BBRP characteristic acceleration is given by:

$$a_{c,BBRP} = \frac{4\pi}{3} \frac{I_{BBRP}}{c\sigma} \tag{21}$$

Although $a_{c,BBRP}$ represents the maximum achievable BBRP acceleration, it should be noted that this situation occurs only for a nadir-pointing solar sail ($\hat{\boldsymbol{n}}_{out} = \hat{\boldsymbol{r}}$, $\alpha_{\oplus} = 0$) at zero altitude. Indeed, in this case $G_F = 1$, see Eq. (17), and $\lVert \boldsymbol{a}_{BBRP} \rVert = a_{c,BBRP}$. Ultimately, it is worth noting that $a_{c,BBRP}$ can also be expressed in terms of the SRP characteristic acceleration, a_c, by substituting Eq. (3) in Eq. (21):

$$a_{c,BBRP} = \frac{2\pi}{3} \frac{I_{BBRP}}{\mathbb{S}_{\oplus}} a_c = 0.1067\, a_c \tag{22}$$

Albedo Radiation Intensity. When the albedo radiation is considered, the radiation intensity, I_{ARP}, depends on the illumination conditions of the visible surface and varies across A^*. Its definition is given by[25]:

$$I_{ARP} = \frac{\Lambda \mathbb{S}_{\oplus}}{\pi} \max\left(0, \cos(\chi)\right) \tag{23}$$

where $\Lambda = 0.36$ is the Earth's albedo, i.e., the average amount of solar radiation received by the Earth reflected into space[25], and χ is the sunlight incidence angle between the reverse sunlight direction, $-\hat{\boldsymbol{l}}$, and $\hat{\boldsymbol{N}}$, see Figure 2c. Because the incidence angle χ varies across the visible surface A^*, I_{ARP} is not constant around the Earth, unlike I_{BBRP}. The varying nature of I_{ARP} significantly increases the complexity of the surface integral of Eq. (13), for which the existence of an analytical solution is not guaranteed. To avoid this problem, this paper proposes a surface-averaged, constant value of the albedo radiation intensity. By doing so, the total amount of albedo radiation emitted by the visible surface A^* is assumed to be irradiated isotropically, i.e., such that any elementary piece of the Earth's visible surface, dA, emits the same amount of radiation, regardless of its local sunlight incidence angle. This assumption implies that I_{ARP} is constant across the visible surface A^* and allows to compute the ARP acceleration in a similar fashion as the BBRP acceleration. Based on Eq. (23), the surface-averaged albedo radiation intensity can be expressed in the following form:

$$\overline{I}_{ARP} = \frac{\Lambda \mathbb{S}_{\oplus}}{\pi} \Phi \tag{24}$$

where the term $\Phi \in [0,1]$ is the surface-averaged cosine of the sunlight incidence angle with respect to the surface A^*, i.e.:

$$\Phi = \frac{\int_{A^*} \max(0, \cos(\chi))\, dA}{\int_{A^*} dA} \tag{25}$$

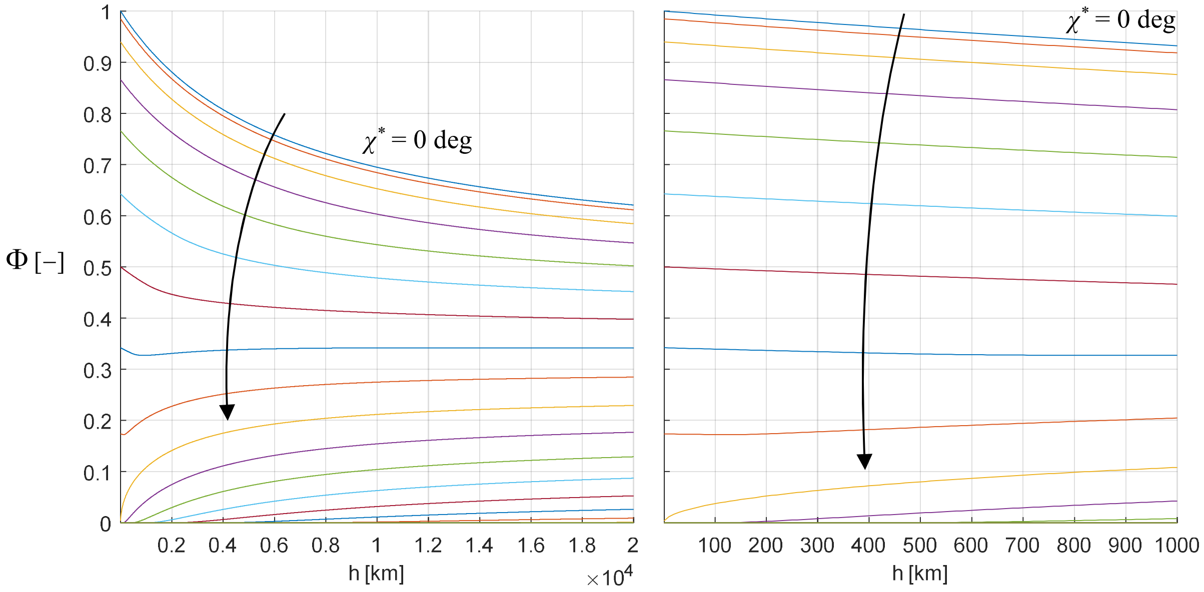

Figure 4. Albedo phase function as a function of altitude for different phase angles. The phase angle increases in the direction of the arrow from 0 to 180 deg with a step size of 10 deg.

Φ is known as albedo phase function in the literature[24] and will be referred to in this way in the following. Employing the constant radiation intensity $\bar{I}_{ARP}$ instead of I_{ARP} in the surface integral of Eq. (13) allows solving it and taking advantage of Eq. (14) to compute $\boldsymbol{a}_{ARP}$. Again, the geometrical factor can be found through Eq. (17)-(19), while the ARP characteristic acceleration is given by:

$$a_{c,ARP} = \frac{4\pi}{3}\frac{\bar{I}_{ARP}}{c\sigma} \tag{26}$$

By using Eq. (3), the value of $a_{c,ARP}$ can also be expressed in terms of the SRP characteristic acceleration as:

$$a_{c,ARP} = \frac{2\Lambda}{3}\Phi\, a_c = 0.24\,\Phi\, a_c \tag{27}$$

Unlike the BBRP characteristic acceleration, the value of $a_{c,ARP}$ is not constant but depends on the term Φ, which accounts for the illumination conditions of the visible surface of the Earth. Indeed, the Earth's visible surface, A^*, can appear either completely illuminated (if the sailcraft "sees" only the sunlit side of the Earth), partially illuminated (if the Earth's day-night terminator is visible from the sailcraft), or completely dark (if the sailcraft "sees" only the dark side of the Earth). These three cases can be identified through the maximum view angle, φ, and the phase angle, $\chi^* \in [0, \pi]$, i.e., the angle between $\hat{\boldsymbol{r}}$ and the opposite to the sunlight direction, $-\hat{\boldsymbol{\imath}}$, see Figure 2c. For each of these cases, analytical expressions can be found for the phase function, Φ, as shown in the following:

a) If $\chi^* < \varphi$, the visible surface A^* is completely illuminated by the Sun. In this case, Φ is equal to:

$$\Phi\left(r,\chi^*\right) = \frac{1}{2}\left(1+\frac{R}{r}\right)\cos(\chi^*) \tag{28}$$

b) If $\varphi < \chi^* < \pi - \varphi$, , the visible surface A^* is partially illuminated by the Sun. In this case, Φ is given by:

$$\begin{aligned}\Phi\left(r,\chi^*\right)=\frac{1}{2\pi}\Bigg\{&\left(1-\frac{R}{r}\right)^{-1}\left[\cos^{-1}\left(\frac{R}{r\sin\left(\chi^*\right)}\right)-\frac{R}{r}\sqrt{\sin^2\left(\chi^*\right)-\frac{R^2}{r^2}}\right]\\&+\left(1+\frac{R}{r}\right)\cos\left(\chi^*\right)\cos^{-1}\left(-\frac{R}{\sqrt{r^2-R^2}}\frac{\cos\left(\chi^*\right)}{\sin\left(\chi^*\right)}\right)\Bigg\}\end{aligned} \qquad (29)$$

c) If $\pi - \varphi < \chi^*$, the visible surface A^* is completely dark and $\Phi = 0$.

In Figure 4, Φ is plotted as a function of the orbital altitude, h, for a range of different phase angles, χ^*. This plot can be used by the reader to easily retrieve the value of Φ for a wide range of configurations, hence allowing to find $a_{c,ARP}$ through Eq. (26)-(27) and compute $\boldsymbol{a}_{ARP}$ through Eq. (14).

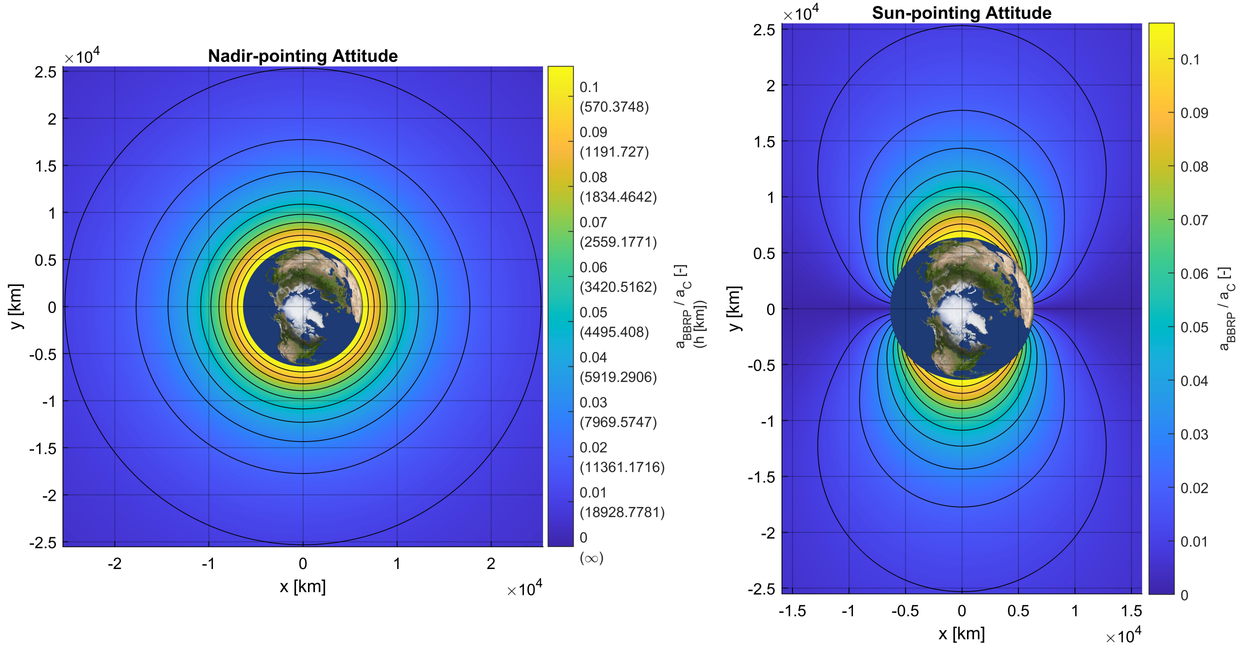

(a) (b)

Figure 5. BBRP acceleration magnitude for a nadir-pointing solar sail (left) and Sun-pointing solar sail (right). The contour line values range from 0.01 to 0.1 with a step of 0.01.

ANALYSIS OF THE BLACKBODY RADIATION PRESSURE ACCELERATION

Figure 5 shows the contour plots of the BBRP acceleration magnitude relative to the solar-sail characteristic acceleration, a_c, in the near-Earth environment for a nadir-pointing solar sail (i.e., $\hat{\boldsymbol{n}}_{out} = \hat{\boldsymbol{r}}$) and Sun-pointing solar sail (i.e., $\hat{\boldsymbol{n}}_{out} = \pm\hat{\boldsymbol{l}}$), respectively. As can be seen in Figure 5a, for a nadir-pointing attitude, the BBRP acceleration magnitude, a_{BBRP}, depends solely on the orbital altitude, h, as the PCA is constant and equal to zero. This allows correlating a_{BBRP} and h, as shown in the legend of Figure 5a. The contour plot shows the rapid decay of a_{BBRP} especially at low altitudes where, nonetheless, accelerations up to 10% of a_c can be achieved, which is in agreement with Eq. (22) and in line with the results found in the literature[13]. Similar to Figure 5a, Figure 5b shows the iso-acceleration curves for a Sun-pointing solar sail, when the Sun is located along the positive y-axis direction. In this case, the acceleration varies less uniformly as the PCA is not constant. In particular, a_{BBRP} is equal to zero on the x-axis, where the sail is oriented edgewise with respect to the radial direction ($\alpha_{\oplus} = \pi/2$). This causes the BBRP accelerations exerted on the sail's front and back sides to counteract each other. Also, it is worth noting that the acceleration profile is symmetric with respect to the x-axis, which is a consequence of the fact that a double-sided perfectly reflecting solar sail has been considered. Indeed, for a solar sail with different optical properties on the front and back sides, no symmetry would be found.

A contour plot showing the whole range of attainable a_{BBRP} values for any possible PCA and a wide range of altitudes appears in Figure 6. The plot shows how a_{BBRP} decreases steeply at low altitudes, displaying a behavior similar to an inverse square law. Increases in the PCA also affect the acceleration magnitude, which drops rapidly until reaching a zero value for $\alpha_{\oplus} = \pi/2$, as previously discussed.

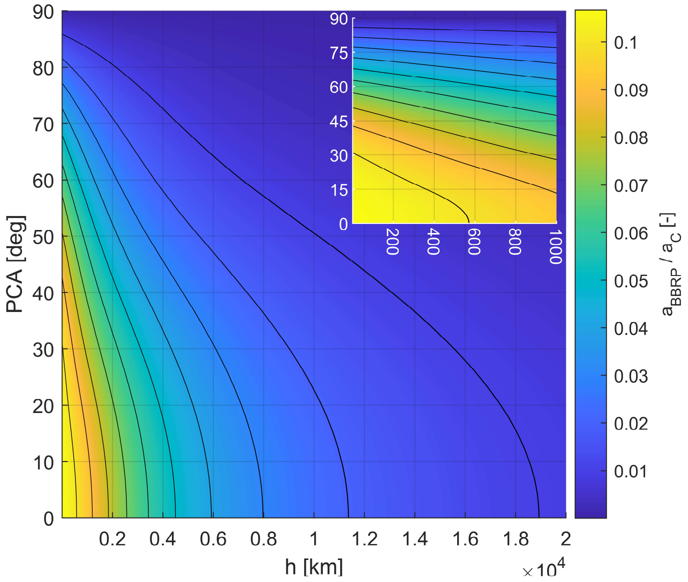

Figure 6. BBRP acceleration magnitude as a function of altitude and PCA. The contour line values range from 0.01 to 0.1 with a step of 0.01.

Comparison with Finite-disk Radiation Source Model

In order to quantify the accuracy of the spherical BBRP acceleration model presented in this article, a comparison against the FD radiation source model devised by McInnes[1] is conducted. This model has been widely applied in the literature[13,14] and assumes the emitting body (the Earth) to irradiate as a uniformly bright disk and solely in the radial direction, $\hat{\boldsymbol{r}}$. As such, it does not take into account the curvature of the Earth and the possibility of having both sides of the sail illuminated simultaneously. When using the FD model, the BBRP acceleration, $\boldsymbol{a}_{BBRP,FD}$, is given by[1,13,14]:

$$\boldsymbol{a}_{BBRP,FD} = a_{c,BBRP} G_{F,FD} \hat{\boldsymbol{n}}_{out} \tag{30}$$

where $G_{F,FD}$ represents the geometrical factor of the FD model:

$$G_{F,FD} = \left[1 - \left(1 - \frac{R^2}{r^2}\right)^{3/2}\right] \cos^2(\alpha_{\oplus}) \tag{31}$$

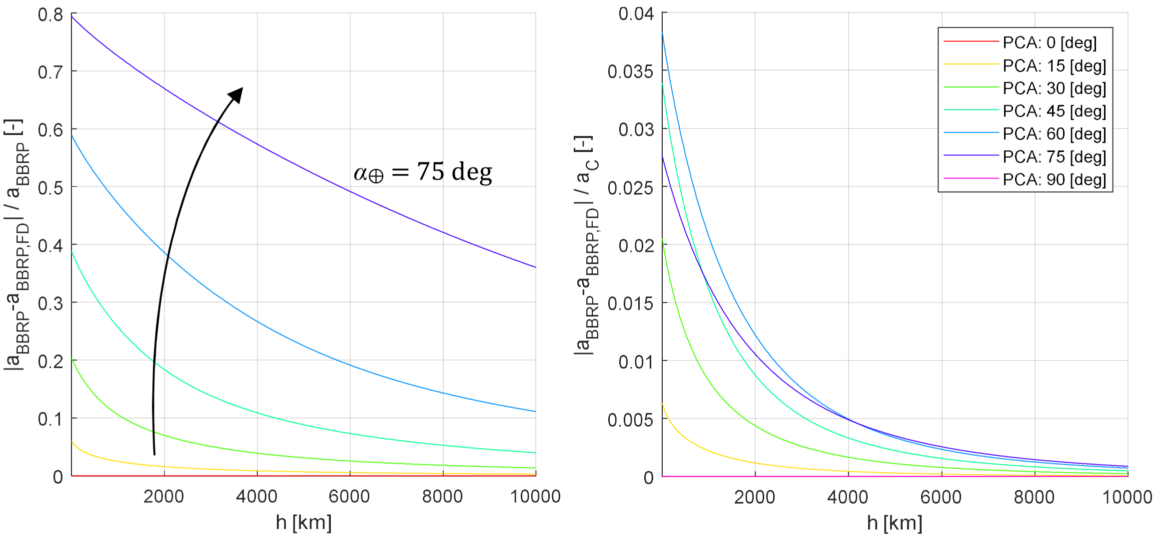

(a) (b)

Figure 7. Relative error (left) and absolute error (adimensionalized with respect to the solar-sail characteristic acceleration, right) between the BBRP accelerations of the spherical and FD models. The PCA increases in the direction of the arrow.

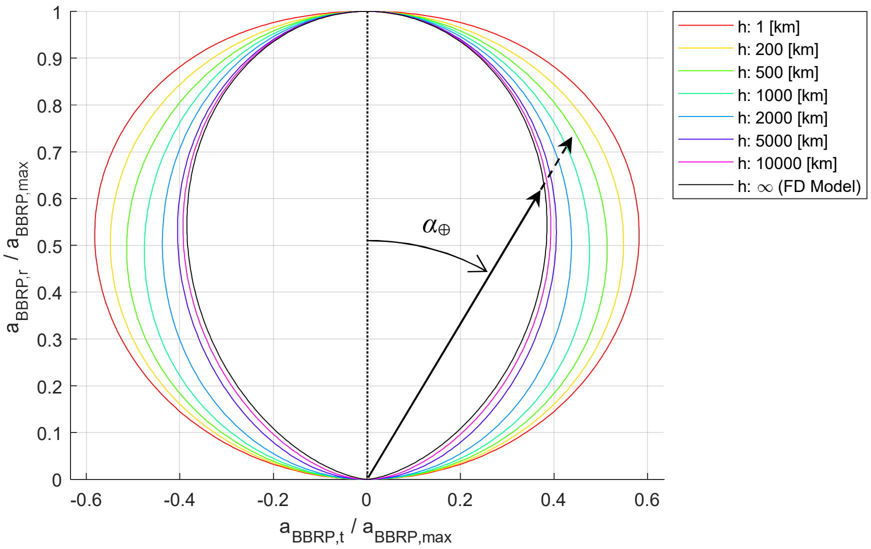

Figure 8. BBRP acceleration envelope curves of the FD and spherical radiation source models. The solid and dashed arrows represent the accelerations of the FD and spherical radiation source models (for *h* = 500 km), respectively.

By comparing Eq. (14), (17), and (18) with Eq. (30) and (31) it can be noted that the only difference between the BBRP accelerations of the spherical model and FD model is given by the definition of the geometrical factors. As such, the comparison of the BBRP accelerations of these two models will also provide direct insights in the difference between G_F and $G_{F,FD}$.

The relative and absolute errors on the BBRP acceleration between the new spherical model and the FD model as a function of altitude and for a range of PCAs are shown in the plots of Figure 7. As can be seen, no absolute error is present when $\alpha_\oplus = 0$. This result is due to the expression of the spherical model's geometrical factor, given in Eq. (17). Indeed, by substituting $\alpha_{\oplus} = 0$ into Eq. (17) the expression for the spherical model's geometrical factor reduces to the FD model's geometrical factor in Eq. (31). Consequently, this also yields equal expressions for the spherical and FD models' accelerations, see Eq. (14) and (30). The two plots also show that for increasing altitudes the absolute and relative errors asymptotically tend to zero. This is a consequence of the fact that for increasingly larger altitudes the error introduced by considering the planet as a uniformly irradiating disk (rather than a spherical radiation source) reduces, thus implying that the spherical model converges to the FD model. Note that this result can also be found analytically. Indeed, by expanding G_F in Eq. (17) in powers of (R/r), considering $R/r \rightarrow 0$ (corresponding to $h \rightarrow \infty$), and ignoring the higher-order terms of the expansion, the expression for $G_{F,FD}$ in Eq. (31) is found. For larger values of the PCA, the relative error between the accelerations of the two models increases rapidly, reaching values even in the order of 80% for low altitudes and high PCAs. The reason for this behavior is better explained in Figure 8, where the acceleration envelope curves of the two models are given. These curves represent the set of all attainable BBRP accelerations achievable when changing the PCA. As can be seen, the spherical model's envelope curve varies its shape depending on the altitude, unlike the FD model (shown in black for $h \rightarrow \infty$). All curves of the spherical model coincide with the FD curve for $\alpha_{\oplus} = 0$, as previously discussed. However, for increasing PCAs, the spherical model's envelope curves show a larger transversal component of the acceleration. These discrepancies with the FD model's envelope curve yield the high relative errors observed in Figure 7a. While the relative error increases monotonically with the PCA, the absolute error shows a more complicated dependency on the PCA, see Figure 7b. As can be seen, the largest absolute errors are found for intermediate values of the PCA. These errors reach values up to 3.5-4% of the characteristic acceleration, for low altitudes. Ultimately, in Figure 8 it is also possible to observe how the spherical model's envelope curves converge to the FD model's envelope curve as the altitude increases, in agreement with the error plots of Figure 7 previously discussed.

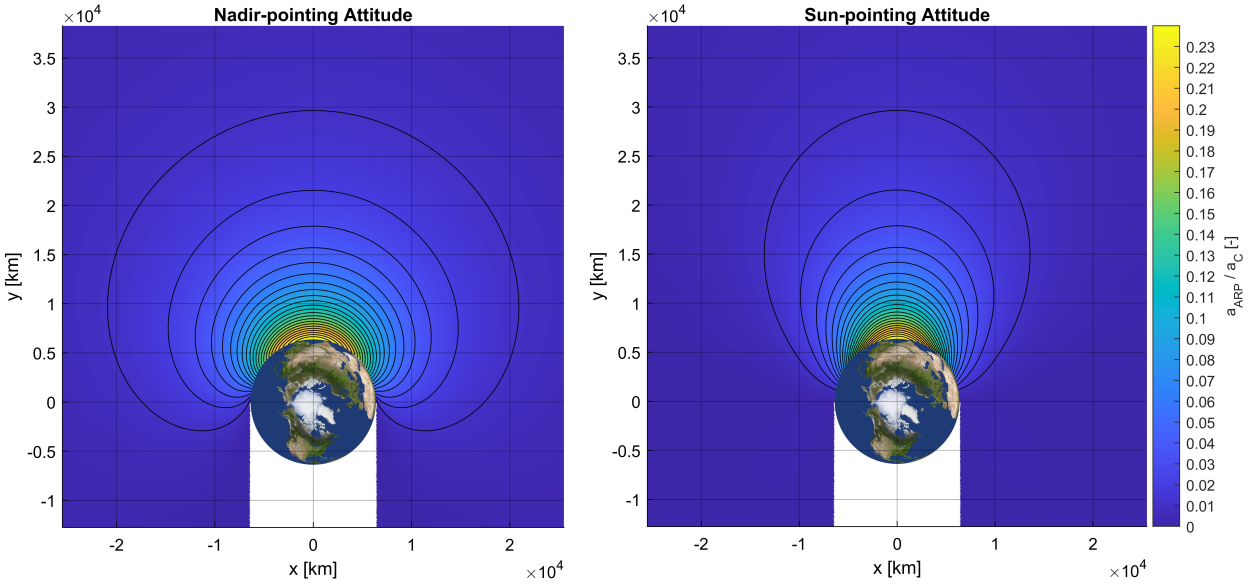

(a) (b)

Figure 9. ARP acceleration magnitude for a nadir-pointing solar sail (left) and Sun-pointing solar sail (right). Contour line values range from 0.01 to 0.23 with a step of 0.01. Eclipse regions are shown in white.

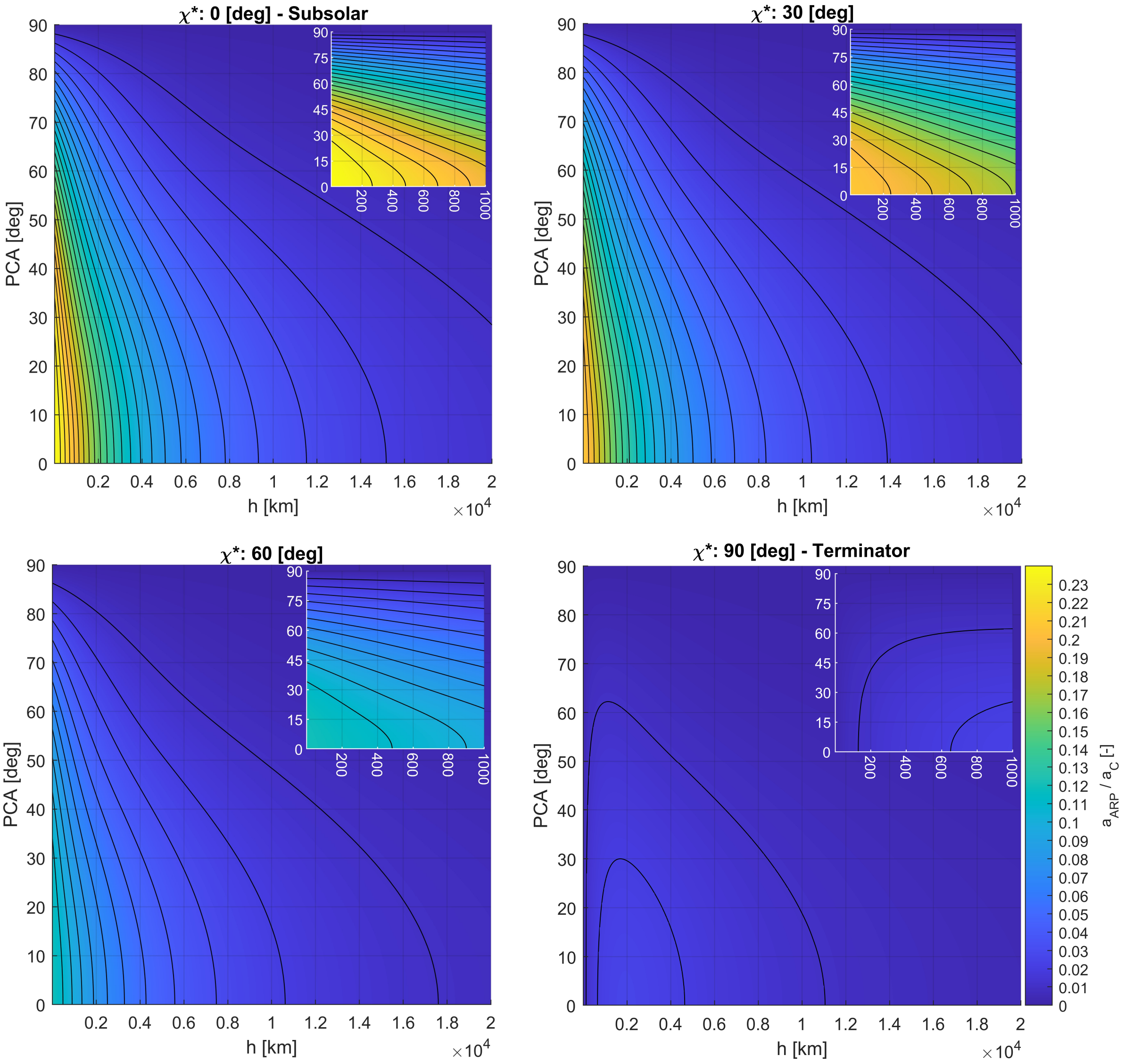

Figure 10. ARP acceleration magnitude as a function of altitude and PCA for different phase angles. The contour lines start at a value of 0.01 and increase with a step of 0.01.

ANALYSIS OF THE ALBEDO RADIATION PRESSURE ACCELERATION

Similar to Figure 5 for the BBRP acceleration, Figure 9 shows the variation of the ARP acceleration magnitude, a_{ARP}, relative to the characteristic acceleration, a_c, for a nadir-pointing and Sun-pointing solar sail. While for the BBRP acceleration the Sun-sail configuration was not of any importance, it is for the ARP acceleration. In both plots of Figure 9, the Sun is placed along the positive y-axis. Compared to the BBRP acceleration, the variation of the ARP acceleration around the Earth for a nadir-pointing sail displays a more complex pattern, due to the additional dependency of a_{ARP} on the phase angle, χ^*. Indeed, Figure 5a shows that large ARP accelerations are achieved when the sail is above the sunlit side of the Earth, reaching values up to 24% of the characteristic acceleration for low altitudes and $\chi^* = 0$, in agreement with Eq. (27). On the other hand, a_{ARP} rapidly decreases when moving towards the dark side of the Earth, eventually reaching the eclipse region where no ARP acceleration is generated. Similar to Figure 5b, Figure 9b displays the variation in ARP acceleration for a Sun-pointing solar sail. In this case, the region of high ARP acceleration shrinks, since moving towards the dark side of the Earth yields increasingly larger PCAs that negatively affect the ARP acceleration magnitude.

In order to better appreciate the variation of the ARP acceleration with the altitude and PCA, Figure 10 shows the contour plots of a_{ARP} as a function of altitude and PCA for different values of the phase angle, χ^*. The plots show that the altitude has a strong influence on a_{ARP} especially for low values of χ^*, in agreement with the results observed in Figure 9. The ARP acceleration also strongly depends on the PCA, as a_{ARP} rapidly reaches zero when approaching a PCA of 90 deg. By increasing the value of χ^*, the correlation between a_{ARP}, h, and PCA changes significantly. In particular, it can be noted that for increasing values of χ^*, the overall achievable a_{ARP} reduces rapidly, shifting its maximum value from 24% to 2% of the characteristic acceleration when varying χ^* from 0 (sub-solar point) to 90 deg (along the terminator). Finally, it is interesting to note that the ARP acceleration for $\chi^* = 90$ deg does not decrease monotonically with altitude, but instead shows an initial increase, followed by a maximum value, and eventually a steady decrease. This behavior is due to two counteracting effects. Indeed, while for increasing altitudes the intensity of the radiation emitted by the Earth decreases, a higher altitude also allows the illuminated part of the Earth visible from the sailcraft to be larger, thus making the sail receive more albedo radiation. Since this latter effect is predominant at low altitudes, an increase in altitude initially yields a larger a_{ARP}. However, for even larger altitudes, the radiation intensity decreases rapidly and its effect becomes predominant, hence making a_{ARP} decrease as well. This non-monotonic behavior of a_{ARP} is evident only when the visible part of the Earth is partially illuminated, i.e., when the day-night terminator is visible from the sailcraft. This is clearly shown also in Figure 9a, where the acceleration contour lines assume a high curvature in proximity of the terminator (which is aligned with the x-axis).

Comparison with Finite-disk Radiation Source Model

Similar to the analysis performed for the spherical BBRP acceleration model, in this section the accuracy of the spherical ARP acceleration model is quantified by comparing it against the FD ARP acceleration model. The ARP acceleration of the FD model can be expressed as[1]:

$$\boldsymbol{a}_{ARP,FD} = a_{c,ARP,FD} G_{F,FD} \hat{\boldsymbol{n}}_{out} \tag{32}$$

where $a_{c,ARP,FD}$ is the albedo characteristic acceleration of the FD model:

$$a_{c,ARP,FD} = \frac{4\pi}{3}\frac{I_{ARP}}{c\sigma} = a_{c,ARP}\frac{\Phi_{FD}}{\Phi} \tag{33}$$

In Eq. (33), Φ_{FD} is the albedo phase function of the FD model, given by:

$$\Phi_{FD} = \max\left(0, \cos\left(\chi^*\right)\right) \tag{34}$$

The above definition of $a_{c,ARP,FD}$ is based on albedo flux models commonly used in the literature[13,25] and differs from $a_{c,ARP}$ only for the use of Φ_{FD} instead of Φ, as highlighted in Eq. (33). As discussed in the following, the different definitions of the phase function and geometrical factor of the spherical and FD models are at the core of the acceleration differences between the two models.

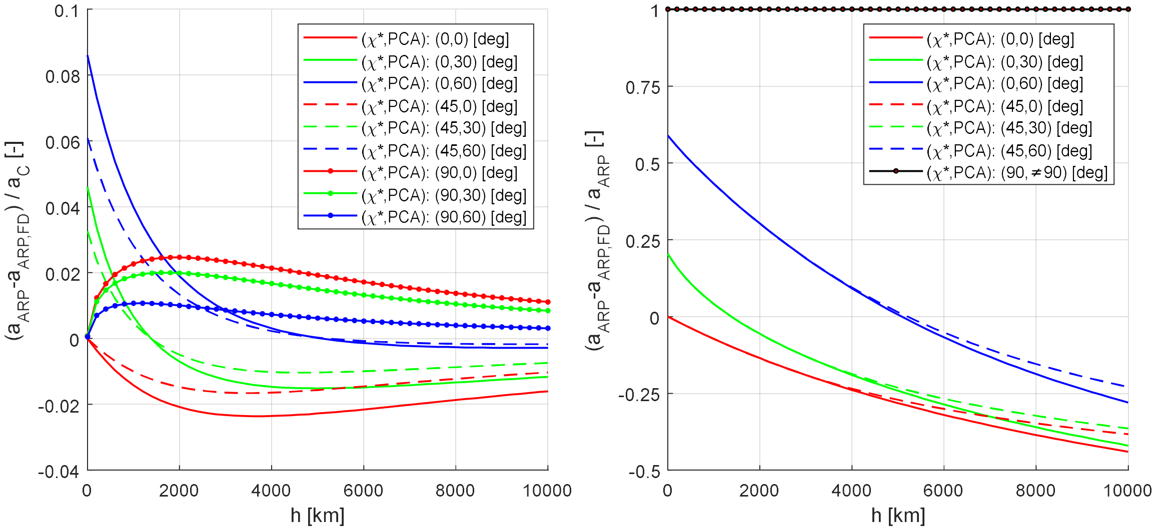

(a) (b)

Figure 11. Error (adimensionalized with respect to the solar-sail characteristic acceleration, left) and relative error (right) of the ARP acceleration of the FD model with respect to the ARP acceleration of the spherical model.

The plots of Figure 11 show the error and relative error of the FD model's ARP acceleration with respect to the spherical model's ARP acceleration as a function of altitude, for a range of PCAs and phase angles. It should be noted that, contrary to Figure 7, in Figure 11 the actual errors are displayed instead of their absolute values. In this way, it is possible to better highlight in which cases the spherical model's acceleration, a_{ARP}, is larger than the FD model's acceleration, $a_{ARP,FD}$, and vice versa. As shown in Figure 11a, when $\chi^* = 90$ deg (i.e., when the sailcraft is above the terminator) the acceleration error is positive for any altitude and PCA, meaning that $a_{ARP} > a_{ARP,FD}$. This result is due to the fact that the FD model's phase function, Φ_{FD}, is equal to zero for $\chi^* = 90$ deg, hence yielding $a_{ARP,FD} = 0$. On the other hand, when the spherical model is employed, a small ARP acceleration, a_{ARP}, is found. As can be seen in the plot, this ARP acceleration is always smaller than 3% of the SRP characteristic acceleration, a_c, and rapidly approaches zero for altitudes below 1000 km. Figure 11a shows that also for $\chi^* = \{0,45\}$ deg and $\alpha_\oplus = 0$ the acceleration error is bounded within 3% of a_c. However, in these cases the error achieved is negative, thus implying $a_{ARP} < a_{ARP,FD}$. Since the geometrical factors of the spherical and FD models are the same for $\alpha_\oplus = 0$, the acceleration error found is introduced solely by the difference in phase function of the two models. For the remaining cases given in Figure 11a, i.e., for $\chi^* = \{0,45\}$ deg and $\alpha_\oplus = \{30,60\}$ deg, the acceleration errors vary more strongly with the altitude, assuming both positive and negative values. In particular, at low altitudes the main source of error is given by the difference in the geometrical factors of the two models, which corresponds to a_{ARP} being larger than $a_{ARP,FD}$ by up to 8% of a_c. For increasing altitudes, the error rapidly drops and even assumes negative values, implying that $a_{ARP,FD} > a_{ARP}$. This happens because for increasing distances from the Earth the error introduced by using different phase functions becomes dominant and causes the FD model to overestimate the acceleration. Finally, it is interesting to note that all error curves asymptotically tend to zero for increasing altitudes, meaning that the FD and spherical models behave similarly at large distances from the Earth. Figure 11b also provides the relative error on the acceleration between the two models. As can be seen, this varies in the range [-50%, 60%] for most cases and even assumes a value of 1 for $\chi^* = 90$ deg, since $a_{ARP,FD} = 0$. This result highlights the different assumptions underlying the two models and the limitations of the FD model to accurately determine the ARP acceleration.

RESULTS AND ANALYSIS

In this section, the effect of the BBRP and ARP accelerations on the orbit-raising and inclination-changing capabilities of different Earth-bound solar-sail orbits is analyzed and discussed. All analyses make use of the ACS3 mission as baseline scenario, with a solar-sail characteristic acceleration of $a_c = 0.045$ mm/s^2, a simulation start time of April 1st, 2023 (i.e., the expected deployment date of the solar sail), and the following vector of initial Keplerian elements defined in frame $I(x, y, z)$:

$$\left[a_0, e_0, i_0, \Omega_0, \omega_0, f_0\right]^T = \left[7093.1363\,\text{km}, 0, 98.2490\,\text{deg}, \begin{Bmatrix} 280.5833\,\text{deg} \\ 10.5833\,\text{deg} \end{Bmatrix}, 0\,\text{deg}, 0\,\text{deg}\right]^T \tag{35}$$

where a is the semi-major axis, e the eccentricity, i the inclination, Ω the right ascension of the ascending node, ω the argument of perigee, f the true anomaly, and the subscript “0” denotes the initial value of these variables[*]. These Keplerian elements represent a circular, Sun-synchronous orbit with initial altitude $h_0 = a_0 - R = 715$ km. As shown in Eq. (35), two different values for the initial right ascension of the ascending node are used: the first corresponds to a local time of the ascending node (LTAN) at 6AM (dawn-dusk orbit) and the second to an LTAN at 12AM (noon-midnight orbit). For each initial orbit, the solar-sail dynamics are propagated and locally optimal orbit-raising and inclination-changing steering laws are employed. These steering laws are computed using an algorithm accounting for both SRP and atmospheric drag in the optimization process[10], but not for the PRP. Therefore, in the following analyses the BBRP and ARP accelerations are considered as uncontrolled perturbing accelerations affecting the orbit. To quantify the effect of these accelerations on the orbit-raising and inclination-changing capabilities of the ACS3 mission, the equations of motion presented in Eq. (1) are propagated with and without PRP acceleration on the right-hand side. In this way, the final increases in altitude and inclination for PRP-perturbed and PRP-unperturbed orbits can be compared and their difference is assessed. For each scenario, the equations of motion are propagated for 10 days using Matlab®’s *ode45* integrator, with absolute and relative tolerances of 10^{-12}. More details on the optimization scheme as well as the settings used for the optimizer are provided in Reference 10.

Figure 12 shows the variation of the SRP, aerodynamic, BBRP, ARP, and total accelerations over one orbital period, for the two steering laws (indicated by “SL” in the figure) and initial LTANs. The large differences in the acceleration profiles for the four cases are due to the different sail attitude control profiles adopted. Indeed, the solar-sail attitude control is computed through the optimization process and strongly depends on the steering law and LTAN considered. For more details on the sail attitude angles profiles, see Reference 10. As shown in the plots, most of the time the SRP acceleration is the dominant acceleration. However, the BBRP and ARP accelerations can get as large as 10-20% of the solar-sail characteristic acceleration and, for some cases and in some particular sections of the orbit, attain values even larger than the SRP acceleration. These large values of the BBRP and ARP accelerations are achieved only when an initial LTAN at 12 AM is considered. Indeed, for an initial LTAN at 6AM, the maximum BBRP and ARP accelerations attain values in the order of 1% of the characteristic acceleration, thus affect-

---

[*] ACS3 mission data taken from personal communication with W.K. Wilkie, Principal Investigator of the ACS3 mission, NASA Langley Research Center, July 2022.

ing the dynamics only slightly. The reason for this lies in the relative orientation of the orbital plane and the optimal sail normal direction, for which the sail is constantly oriented almost edgewise with respect to the Earth's radial direction. This causes the accelerations of the sail's front and back sides to counteract each other, thus yielding an almost null net PRP acceleration. It is interesting to note that when an LTAN at 12AM and an orbit-raising steering law are considered, a similar effect is achieved also during eclipses. Indeed, in this case the normal vector of the sail is oriented perpendicular to the orbital plane. This translates into the sail being oriented parallel to the wind flow (to prevent atmospheric drag) and, once again, the BBRPs on the sail front and back sides counteracting each other to produce a null net acceleration. In addition, because the sail is in eclipse, no solar radiation or albedo is present, thus making the total acceleration exerted on the sail equal to zero.

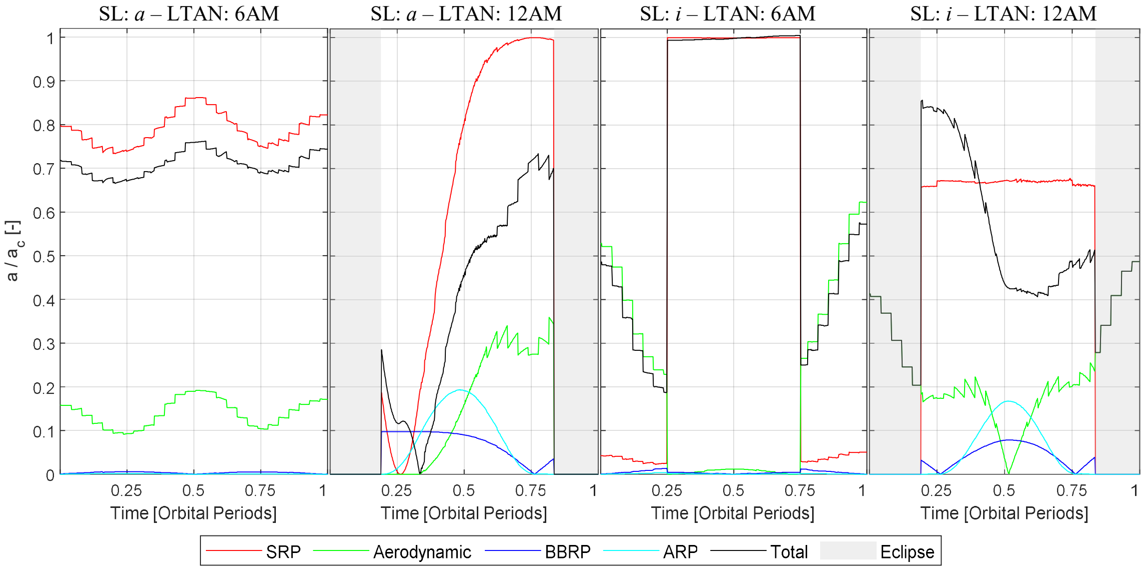

Figure 12. ACS3 acceleration profiles over one orbital period for the orbit-raising steering law (SL: *a*) and inclination-changing steering law (SL: *i*) and for LTANs at 6AM and 12AM.

Table 1 displays the maximum BBRP and ARP accelerations achieved and the altitude and inclination increases obtained after 10 days, for all orbit scenarios, with and without PRP in the dynamics. In the table, $\Delta œ_{0\rightarrow f}$ is the achieved increase in the steering law's target parameter (i.e., *h* or *i*) after 10 days, $\epsilon_{f,abs}$ represents the absolute error in the final value of the target parameter when no PRP is considered in the dynamics, and $\epsilon_{f,rel}$ is the corresponding relative error (computed with respect to the value of $\Delta œ_{0\rightarrow f}$ with PRP). As observed also in Figure 12, the maximum BBRP and ARP accelerations are considerably smaller for an LTAN at 6AM than an LTAN at 12AM. Therefore, for an LTAN at 6AM the effect of the PRP on the orbit-raising/inclination-changing capabilities of the sail is only minor. This translates into relative errors in the altitude/inclination change smaller than 1% with respect to the case in which the PRP is not accounted for. On the other hand, for an LTAN at 12 AM, large BBRP and ARP accelerations are found, yielding absolute errors with respect to the case without PRP of 2.53 km (orbit-raising steering law) and $9.61 \cdot 10^{-3}$ deg (inclination-changing steering law). These correspond to large relative errors, equal to 19.63% and 25.02%, respectively. Finally, it is interesting to note that for the inclination-changing steering law with an LTAN at 6AM a slightly higher inclination increase is achieved when the PRP is considered in the dynamics, despite the fact that the PRP is not accounted for in the optimization process. This indicates that the PRP acceleration can work in favor of the inclination increase and that accounting for the PRP acceleration in the optimization procedure may enable solar sails to achieve even larger inclination changes than foreseen to date[14].

Table 1. ACS3 simulation results for a simulation duration of 10 days, for different steering laws, initial LTANs, and orbital dynamics with and without PRP.

Steering Law	Orbit raising				Inclination changing			
LTAN	6AM		12 AM		6 AM		12 AM	
PRP	✗	✓	✗	✓	✗	✓	✗	✓
$\frac{a_{BBRP,max}}{a_c}$ [%]	N/A	1.42	N/A	9.77	N/A	4.49	N/A	7.85
$\frac{a_{ARP,max}}{a_c}$ [%]	N/A	0.59	N/A	19.45	N/A	1.62	N/A	16.77
$\Delta œ_{0\rightarrow f}$ [km, deg]	21.50	21.47	15.41	12.88	$9.56\cdot10^{-2}$	$9.58\cdot10^{-2}$	$4.80\cdot10^{-2}$	$3.84\cdot10^{-2}$
$\epsilon_{f,abs}$ [km, deg]	0.03		2.53		$1.97\cdot10^{-4}$		$9.61\cdot10^{-3}$	
$\epsilon_{f,rel}$ [%]	0.15		19.63		0.21		25.02	

CONCLUSIONS

In this paper, a novel analytical model for the blackbody radiation pressure (BBRP) and albedo radiation pressure (ARP) accelerations has been presented, valid for any planet and for double-sided perfectly reflecting solar sails. The dynamics of a solar sail in the near-Earth environment have been presented, including the solar radiation pressure, aerodynamic, BBRP, and ARP accelerations. In particular, special focus has been given to the BBRP and ARP accelerations, whose underlying assumptions and analytical derivation have been provided. It has been shown that these accelerations depend solely on the sail attitude, distance from the planet, and Sun-planet-sailcraft angle through two functions, namely the geometrical factor and albedo phase function. In order to quantify the achievable BBRP and ARP accelerations in the near-Earth environment, a thorough analysis of their magnitudes for a variety of conditions has been presented and discussed. The results show that BBRP and ARP accelerations in the order of 10% and 20% of the solar-sail characteristic acceleration can be achieved, respectively. To assess the accuracy of the BBRP and ARP acceleration models presented in this paper, comparisons against the finite-disk radiation source model devised by McInnes have been conducted. These show that absolute errors in the BBRP acceleration and ARP acceleration up to 3.5-4% and 8% of the solar-sail characteristic acceleration can be achieved, respectively, particularly for low altitudes and for intermediate solar-sail cone angles and Sun-Earth-sailcraft angles. To show the perturbing effect of the planetary radiation pressure acceleration on the orbit-raising and inclination-changing capabilities of solar sails in LEO, different analyses have been conducted using NASA's upcoming ACS3 mission as baseline scenario. These analyses show the non-negligible effect of an uncontrolled planetary radiation pressure acceleration, which can yield losses in the altitude gain up to 2.53 km over a 10 day orbit-raising period, equivalent to 19.63% of the total altitude gain. In a similar fashion, when an inclination-changing steering law is implemented, losses in the inclination gain of $9.61\cdot10^{-3}$ deg are observed after 10 days, corresponding to 25.02% of the total inclination gain.

ACKNOWLEDGMENT

The authors thank W. Keats Wilkie from NASA Langley Research Center and Andrew Heaton from NASA Marshall Space Flight Center for fruitful discussions on the ACS3 mission and valuable information shared.

REFERENCES

[1] C. R. McInnes, Solar Sailing - Technology, Dynamics and Mission Applications, Springer, 2004.

[2] D.A. Spencer, L. Johnson, and A.C. Long, “Solar sailing technology challenges,” *Aerospace Science and Technology*, vol. 93, 2019. DOI: 10.1016/j.ast.2019.07.009

[3] M. Macdonald and C.R. McInnes, “Solar sail science mission applications and advancement,” *Advances in Space Research*, vol. 48, no. 11, pp.1702-1716, 2011. DOI: 10.1016/j.asr.2011.03.018

[4] W.K. Wilkie, J.M. Fernandez, O.R. Stohlman, et al., “An overview of the NASA advanced composite solar sail (ACS3) technology demonstration project,” in *AIAA Scitech 2021 Forum*, 2021.

[5] J. Pezent, R. Soon, and A. Heaton, “High-fidelity contingency trajectory design and analysis for NASA’s near-Earth asteroid (NEA) scout solar sail mission,” *Acta Astronautica*, . vol. 159, pp. 385-396, 2019. DOI: 10.1016/j.actaastro.2019.03.050.

[6] N. Miguel and C. Colombo, “Planar Orbit and Attitude Dynamics of an Earth-orbiting Solar Sail under J2 and Atmospheric Drag Effects,” in *AAS/AIAA Astrodynamics Specialist Conference*, Snowbird, Utah, USA, 2018.

[7] N. Miguel and C. Colombo, “Deorbiting Spacecraft with Passively Stabilised Attitude using a Simplified Quasirhombic-pyramid Sail,” *Advances in Space Research,* vol. 67, no. 9, pp. 2561-2576, 2021. DOI: 10.1016/j.asr.2020.03.028

[8] C. Colombo, A. Rossi, F. Dalla Vedova, V. Braun, B. Bastida Virgili, and H. Krag, “Drag and Solar Sail Deorbiting: Re-entry Time Versus Cumulative Collision Probability,” in *68th International Astronautical Congress*, Adelaide, Australia, 2017.

[9] A. Ionel, “Deorbiting Upper-stages in LEO at EOM using Solar Sails,” *INCAS BULLETIN,* vol. 9, no. 2, pp. 117-132, 2017. DOI: 10.13111/2066-8201.2017.9.2.9

[10] L. Carzana, P.N.A.M. Visser, and M.J. Heiligers, “Locally optimal control laws for Earth-bound solar sailing with atmospheric drag,” *Aerospace Science and Technology*, vol. 127, 2022. DOI: 10.1016/j.ast.2022.107666

[11] G. Mengali and A.A. Quarta, “Near-Optimal Solar-Sail Orbit-Raising from Low Earth Orbit,” *Journal of Spacecraft and Rockets,* vol. 42, no. 5, pp. 954-958, 2005. DOI: 10.2514/1.14184

[12] V. Stolbunov, M. Ceriotti, C. Colombo, and C. R. McInnes, “Optimal Law for Inclination Change in an Atmosphere Through Solar Sailing,” *Journal of Guidance, Control, and Dynamics,* vol. 36, no. 5, pp. 1310-1323, 2013. DOI: 10.2514/1.59931

[13] A. De Iuliis, F. Ciampa, L. Felicetti, and M. Ceriotti, “Sailing with Solar and Planetary Radiation Pressure,” *Advances in Space Research*, vol. 67, no. 9, pp.2795-2811, 2021. DOI: 10.1016/j.asr.2019.11.036

[14] A. Barles, M. Ceriotti, F. Ciampa, and L. Felicetti, “An Optimal Steering Law for Sailing with Solar and Planetary Radiation Pressure,” *Aerospace Science and Technology,* vol. 118, 2021. DOI: 10.1016/j.ast.2021.107051

[15] F.G. Cunningham, “Power Input to a Small Flat Plate from a Diffusely Radiating Sphere, with Application to Earth Satellites,” in *NASA Technical Note D-710*, July 1961.

[16] F.G. Cunningham, “Power Input to a Small Flat Plate from a Diffusely Radiating Sphere with Application to Earth Satellites: The Spinning Plate,” in *NASA Technical Note D-1545*, February 1963.

[17] F.G. Cunningham, “Earth reflected solar radiation incident upon an arbitrarily oriented spinning flat plate,” in *NASA Technical Note D-1842*, July 1963.

[18] J. R. Wertz and W. J. Larson, Space Mission Analysis and Design, El Segundo: Microcosm Press and Dordrecht: Kluwer Academic Publishers, 2005.

[19] C.R. Ortiz Longo and S.L. Rickman, Method for the Calculation of Spacecraft Umbra and Penumbra Shadow Terminator Points, NASA Center for Aerospace Information, Linthicum Heights, 1995.

[20] P. Kelly and R. Bevilacqua, “An optimized analytical solution for geostationary debris removal using solar sails,” *Acta Astronautica*, vol. 162, pp. 72-86, 2019. DOI: 10.1016/j.actaastro.2019.05.055

[21] E. Tiesinga, P.J. Mohr, D.B. Newell, and B.N. Taylor, “CODATA recommended values of the fundamental physical constants: 2018,” *Reviews of Modern Physics,* vol. 93, 2021. DOI: 10.1103/RevModPhys.93.025010

[22] J.A. Storch, Aerodynamic Disturbances on Spacecraft in Free-molecular Flow, El Segundo: The Aerospace Corporation, 2002.

[23] B.W. Carroll and D.A. Ostlie, An Introduction to Modern Astrophysics, Pearson, 2014.

[24] J.J. Lissauer and I. de Pater, Fundamental Planetary Science: Physics, Chemistry and Habitability, Cambridge University Press, 2013.

[25] E. Thornton, Thermal Structures for Aerospace Applications, American Institute of Aeronautics and Astronautics, 1996.